

A 2.4 GHz Coplanar Solar Cell Patch Antenna with a Semi-Analytical Evaluation of Temperature Effects

Eduardo V. V. Cambero^{1,2}, Vinícius S. Silva¹, Humberto P. Paz¹, Renan T. Doria¹,
Ivan R. S. Casella¹, Carlos E. Capovilla¹

¹Universidade Federal do ABC (UFABC), Av. dos Estados 5001, Santo André, SP, Brasil,

²currently with IT'IS Foundation, Zurich, Switzerland,

valdes@itis.swiss vinicius.santana@ufabc.edu.br, humberto.paz@ufabc.edu.br, renan.trevisoli@ufabc.edu.br,
ivan.casella@ufabc.edu.br, carlos.capovilla@ufabc.edu.br

Abstract— Solar cells integrated with antennas have aroused scientific interest as an attractive energy source alternative in low power devices for IoT and Wireless Sensor Network applications. Since the space for all components in the systems is scarce, different integration ideas have been proposed in this field. However, further analysis of the performance of photovoltaic modules used as structural components of antennas is still lacking. In this context, this work experimentally extracts the necessary parameters to create an equivalent circuit model of a modified solar cell used as a radiator of a 2.4 GHz coplanar patch antenna. The obtained model is then used in the numerical characterization of the Current-Voltage (I-V) curves under temperature variations. Antenna design and performance are described, and the physical modifications of a commercial solar cell used in the prototype are presented. The I-V curves were generated for temperatures ranging from 243 to 325 K. The obtained simulation results within this temperature range showed a 150 mV shift of the optimal operation point, decreasing in approximately 20 mW the supported power with the temperature rise. A predictive methodology is introduced to estimate the possible values for the fill factor, energy conversion efficiency, and current density in a modified solar cell under temperature variations, allowing a fully operational photovoltaic antenna design.

Index Terms— Coplanar Patch Antenna, Solar Cell, Temperature analysis.

I. INTRODUCTION

Recently, Solar Cells (SC) have been used to eliminate batteries or, at least, extend their period of operation for low power applications in the Internet of Things (IoT) and Wireless Sensor Networks (WSN) [1]. One of the challenges for the use of SC in these systems is the need for small wireless devices, which can be designed through a high level of integration of electronic circuits and the use of new materials and manufacturing techniques [2]. The intrinsic characteristics of these new devices also led to a different approach, based on the integration of the SC and antenna in the same structure [3]–[6]. This integration is not trivial and presents new challenges related to an efficient design of SC Antennas (SCA), where the primary concern is to avoid a severe degradation in the figures of merit of one part (SC or antenna) due to the operational requirements of the other [7].

The SC figure-of-merits can be analyzed by direct characterization of its I-V curves, extracted under Standard Test Conditions (STC) [8], [9]. STCs establish that the extraction of the I-V curves must be performed with an Air Mass coefficient (AM) = 1.5, an irradiance of 1000 W/m², and a temperature of 25°C (considered here, for simplicity, as 298 K). The performance of SCs can be affected in different manners when integrated with antennas. Some of the most common problems are the shadowing effect of the radiating elements [10], the variation of the photovoltaic surface of Commercial SC (CSC) [6], [11], and the reduction of light reaching the SC surface caused by the reflection process on the transparent conductive materials located over the SC structure [12].

All these drawbacks decrease the Power Conversion Efficiency (PCE) and the SC's Fill Factor (FF). For instance, in [13] the PCE was analyzed by comparing the influences of an AF32 cover glass, a solid patch, and a meshed patch over the photovoltaic surface, resulting in PCE decrease of 3%, 5%, and 3.6%, respectively. In [8], a reduction of 3.6% of the silicon surface area imposed approximately 15.6% less current at the Maximum Power Point (MPP). In addition, in [9], the authors analyzed the influence of the area variation of a SC used as the radiating element, attending to PCE, FF, and Current Density (J). It was verified that an area reduction of 238.55 cm² (97%) in the CSC Black 21 NS6QL [14] brings, approximately, a 50% decrease in the PCE. As can be noted, several references analyze the effect of the irradiance level variation and the photovoltaic area reduction on the SCAs [8], [9], [13]. However, there is a lack of studies analyzing the temperature variation effect on the photovoltaic performance of SCAs. The temperature is another critical parameter that can act directly on MPP in I-V curves disturbing the PCE and FF, which justifies the necessity of its scientific investigation.

In low-power applications, small parameters shifts may bring the source output voltage below the optimal operation conditions, degrading the entire system's performance. Therefore, the influence of a temperature variation over the SC MPP represents an essential issue in the characterization of the SCA performance. In this context, according to the authors' knowledge, this work is the first to analyze the effects of temperature variation on the performance of a designed SCA prototype. The workflow of the methodology applied is as follows: the authors experimentally extracted the I-V curves of a modified CSC. Then, from these new curves, the authors analytically obtained the input variables for running a Gauss-Seidel algorithm [15] and got the SC's one-diode equivalent circuit model simulated on Advanced Design Systems (ADS) software. The validation of the simulated model is done by comparing the experimental and numerical obtained I-V curves. Finally, the circuit model was used to produce one I-V curve for each temperature value studied.

In addition to this Introduction, Section II shows the design of a SC patch antenna and how the CSC dimensions were modified to achieve resonance at 2.45 GHz. Section III explains the methodology followed in the temperature analysis of the SCA, starting with the experimental extraction of the SC equivalent circuit model. In contrast, Section IV presents and discusses the obtained results. Finally, Section V exposes the conclusions of the work.

II. SOLAR CELL COPLANAR PATCH ANTENNA DESIGN

Commonly, a coplanar microstrip patch antenna is composed of a thin substrate with one copper layer on the dielectric material, and it has a radiator element with different configurations, such as square, rectangular, circular, among others [16], [17]. However, circular and rectangular configurations are the most commonly used due to their advantages of low complexity in the analysis and easy

fabrication [18]. In the antenna analyzed here (which was proposed by the authors in [6]), the copper layer of the substrate, conventionally used as the rectangular radiator, is substituted by the rear aluminum layer of a SC. Since the resonant characteristic is directly related to the radiator size, the dimensions of a CSC are modified to achieve resonance within the 2.4 GHz ISM (Industrial, Scientific, and Medical) band. Hence, this section explains the re-sizing process, including the experimental characterization of the studied SC Coplanar Patch Antenna (SC-CPA).

Before starting the design and fabrication of the SC-CPA, a typical Coplanar Patch Antenna (CPA) prototype was designed for comparison, taking into account main antenna performance parameters, specifically the gain, bandwidth, reflection coefficient, directivity, and radiation efficiency. The reference prototype helps to validate the experimental results of the SC-CPA. The antenna design started by choosing the operating frequency band of interest, which was the 2.4 GHz ISM band in this work. The substrate used to fabricate the antenna structure is a low-cost FR-4 plate with $h = 1.6$ mm, $\epsilon_r = 4.5$, and $\tan\delta = 0.018$.

The CPA adopted layout is shown in Fig. 1. The dimensions were obtained through the classic coplanar patch design method [16]. The values of the variables depicted in the figure are $W = 67$ mm and $L = 45$ mm for the substrate sizes, being $W_p = 32.5$ mm, $L_p = 22$ mm the radiator dimensions. The feedline parameters are $W_f = 3$ mm and $L_f = 11.5$ mm. The gap (g) between the radiating elements and the coplanar ground plane was optimized as wider as possible (in this case, 3 mm). This requirement was necessary due to the fabrication uncertainties in the next step, the SC-patch-radiator fabrication process. Hence, in the case of a very narrow g , those size variations can degrade the $|S_{11}|$ performance of the SC-CPA.

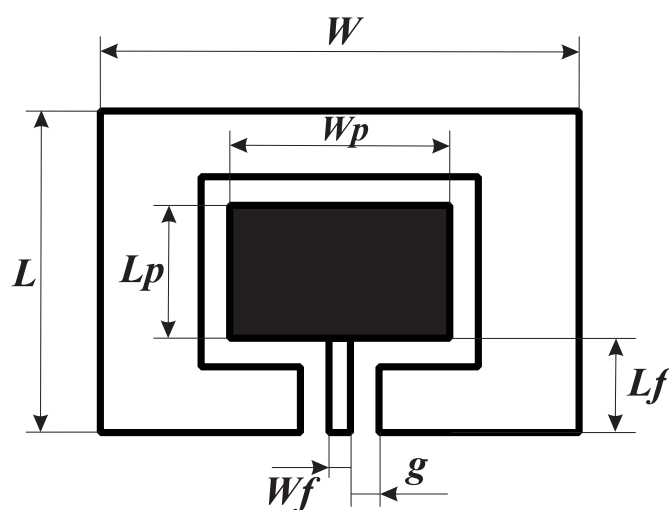


Fig. 1. Dimensions of the CPA. The black color corresponds to the rectangular path radiator. The closed contour in white represents the feedline and the coplanar ground plane, which is separated by a 3 mm gap (g) from the radiator.

The SC-CPA was designed using the exact dimensions obtained for the CPA for a fair comparison. The feedline and the ground plane are implemented with the copper top layer of the FR4 substrate plate. In contrast, the typical copper patch radiator was removed from the substrate (by corrosion with iron perchlorate) and replaced by a rectangular piece of SC, with its rear metal contact used as patch radiator, as can be seen in Fig. 2. The copper feedline is soldered to the rear SC layer using a silver paste and adequately isolated from the SC front bus terminal. The piece of SC was trimmed off from

a commercially available monocrystalline photovoltaic cell from the brand NS6QL Black 21 [14]. The patch radiator of the SC-CPA needed to be trimmed using a rotary tool (Dremel 3000) for crystalline materials, procedures that can carry out minor deviations of the radiator's dimensions from the original values (variations of approximately 1 mm) during the SC patch radiator cutting step.

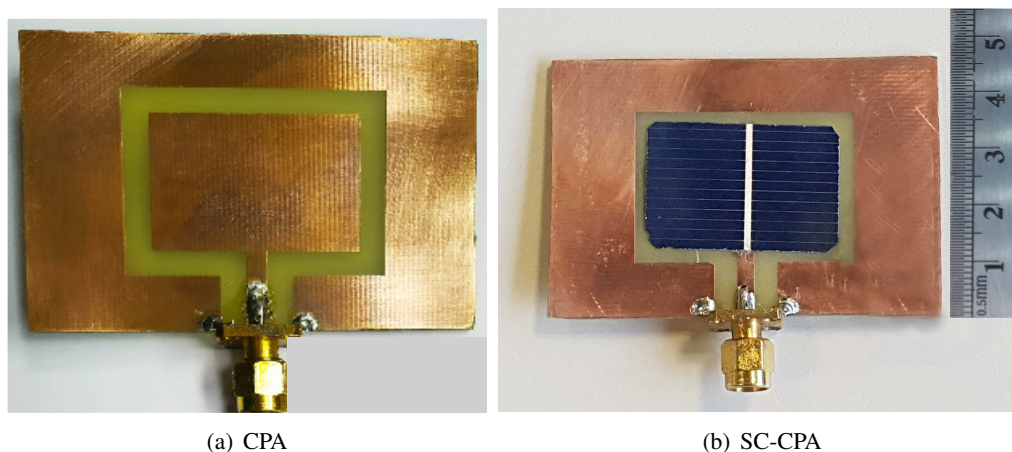


Fig. 2. CPA and SC-CPA prototypes.

A. Reflection Coefficient and Bandwidth Analysis

Both curves in Fig. 3 describe a measured deep in the S_{11} parameters around 2.45 GHz, as expected in the design. The measured bandwidths of the CPA and SC-CPA are, respectively, 270 MHz and 310 MHz, which represent 11% and 12.7% of the operation frequency (according to the $S_{11} \leq -10$ dB criterion) and ensure complete coverage of the 2.4 GHz ISM band. It is important to note that resonant antennas like coplanar patches have a narrow-band characteristic. However, the coplanar waveguide feeding techniques can slightly increase the operation bandwidth [19]. The results endorse the similarity observed between the reflection coefficient curves of the CPA and SC-CPA, justifying the affirmation that a substrate cooper layer substitution by a SC as radiator has not a significant influence on the final antenna's performance associated with the $|S_{11}|$ parameters.

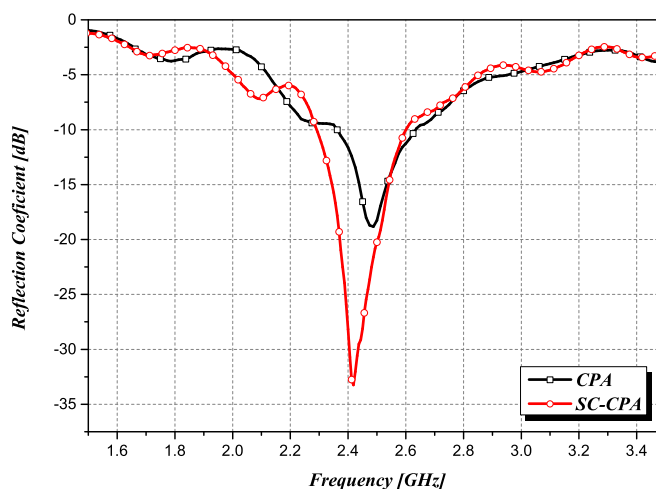


Fig. 3. $|S_{11}|$ measurements results.

B. Radiation Pattern Characteristics

The measured radiation patterns at 2.45 GHz were obtained in the ETS-Lindgren anechoic chamber of the Information and Communication Laboratory (LIC) of the Federal University of ABC (UFABC). The CoPol radiation patterns of the E and H-planes produced by the CPA and the SC-CPA are shown in Fig. 4. In both cases, the measured radiation patterns have a typical coplanar patch characteristic, being satisfactorily similar, resulting from the prototypes' proper design and fabrication process.

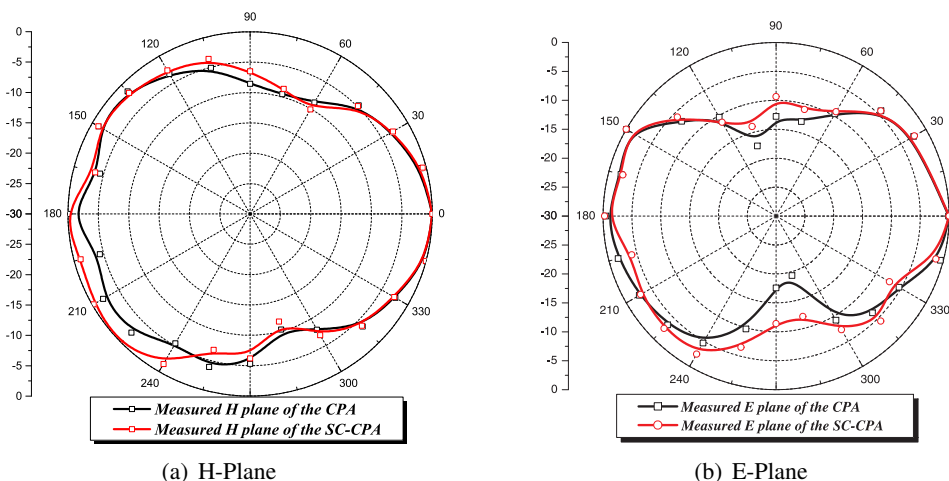


Fig. 4. Radiation pattern results of the CPA and the SC-CPA at 2.45GHz.

The directivity, gain, and radiation efficiency results of the CPA and the SC-CPA at 2.45 GHz, given by the anechoic chamber software, are summarized in Table I, in addition to the bandwidth values in MHz. All corresponding parameters measured from both antennas are very close, confirming the high similarity between the designs, despite the differences in the used radiator elements.

TABLE I. MEASUREMENT RESULTS OF THE MAIN ANTENNA'S PARAMETERS.

Antenna	Bandwidth [MHz]	Directivity [dBi]	Gain [dBi]	Radiation Efficiency [%]
CPA	270 (11.01%)	6.23	4.30	63.60
SC-CPA	310 (12.70%)	6.15	4.19	63.60

III. SC PARAMETERS EXTRACTION IN SC-CPA

In practice, a SC can be analyzed by looking at the corresponding I-V curves and its equivalent circuit schematic shown in Fig. 5. In this figure, an ideal current source is connected in parallel to the diode, representing the recombination current in the quasi-neutral region of the PN junction. On the other hand, I-V curves characterize the SC performance under given irradiance levels through parameters like the PCE or the FF. As shown in (1), FF can be represented by the ratio between the maximum power supplied by a SC and the product between I_{sc} and V_{oc} [1]. In addition, the PCE (2), which is commonly used to assess the performance of energy sources, is defined for a SC as the ratio between the maximum power delivered and the total radiation power received by the photovoltaic surface.

$$FF = \frac{I_{mp}V_{mp}}{I_{sc}V_{oc}} \quad (1)$$

$$PCE = \frac{I_{mp}V_{mp}}{GA_{pvs}} \quad (2)$$

Here G is the irradiance at operation condition, and A_{pvs} is the area of a SC exposed to the light. J is implicitly present in 2 as the ratio between the current and the SCA photovoltaic area.

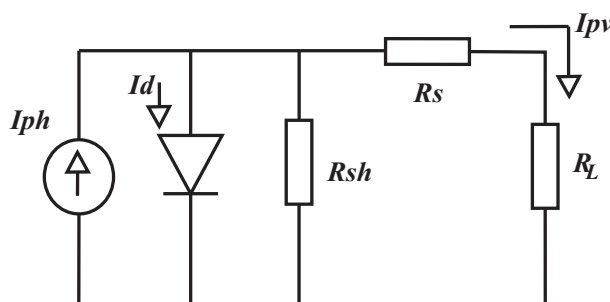


Fig. 5. One-diode equivalent circuit model of the SC.

The SC-CPA analyzed in this work was prototyped by reducing the area of the NS6QL Black 21 from 156.75x156.75 mm [14] to 32.5x22 mm. After the photovoltaic area reduction, the characteristics of the new SC lost the correspondence with the information of the datasheet supplied by the manufacturer, which is fundamental for any design process. Thus, it was necessary to obtain new I-V curves under STC. Fig. 6 shows the used measurement setup, where the Newport 96000 solar simulator was configured to produce the light beam based on the standard AM 1.5 spectra of ASTM E892.

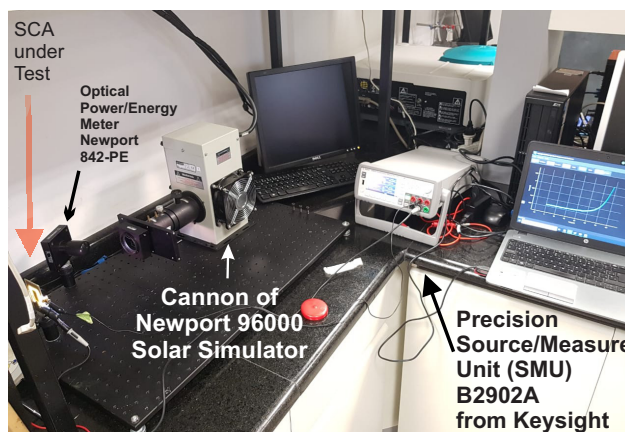


Fig. 6. Experimental setup for the SC evaluation.

The one-diode SC equivalent circuit model was created by using the parameters extracted from the experimental curves through the Gauss-Seidel algorithm [15]. The flowchart of the extraction algorithm is presented in Fig. 7, where w is the iterative weight, A is the ideality factor of the diode junction in the photovoltaic material, T is the absolute temperature of the silicon, e_{max} is the maximum acceptable error, i is the iterations number, i_{max} is the maximum number of iterations, and $e(R_s, R_{sh}, A)$ is the error of each parameter. Also, V_{mp} and I_{mp} are the current and voltage at the maximum power point

(MPP), respectively, while V_{oc} and I_{sc} are the open-circuit voltage and the short-circuit current values. In addition, this algorithm requires an initial estimate of the SC series resistance (R_s) and SC shunt resistance (R_{sh}) to initiate the iterative process and determine the rest of the magnitudes for completing the model. Since datasheet values are no longer valid due to changes in the CSC area, the initial values of R_s and R_{sh} can be considered as the ideal zero and infinity, respectively.

As initial guess of w , it was assumed a value lower than 1 in the early iterations, being decreased when the algorithm reaches local optimum values [20], considering that lower values may imply into slower convergence time, though with lower error oscillations. Therefore, w was initialized as 0.1, and then it is adjusted to 0.05, using 20 times e_{max} as the criterion for the weight variation. In each cycle, A (ideality factor), R_s , and R_{sh} are evaluated through:

$$Y_{k+1} = (1 - w)Y_{k-1} - wY_k \quad (3)$$

where each variable is represented by Y , and Y_k is the variable value in the iteration k .

To clarify the analysis, Table II summarizes all the results obtained after the measurements and the extraction process described in Fig. 7. These parameter values allow defining the equivalent circuit used in the SC temperature variation simulation analysis and subsequent analysis of the SCA behavior.

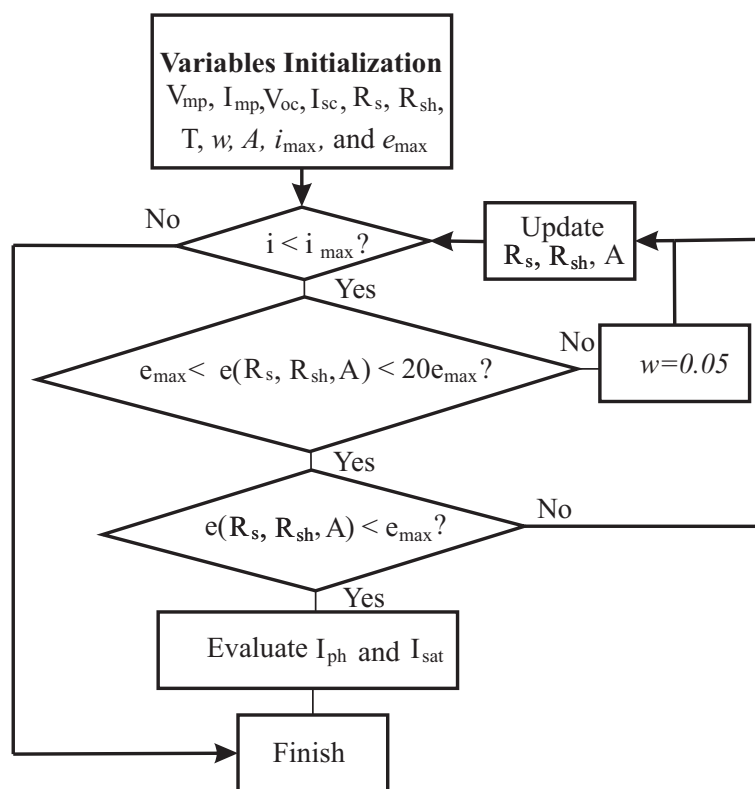


Fig. 7. Modified Gauss-Seidel algorithm.

TABLE II. EXTRACTED SC PARAMETERS UNDER STC.

Irradiance @ 1000 W/m ²		SC-CPA	
Operation Conditions	I_{sc} [mA]	188	
	V_{oc} [mV]	590	
	MPP	I_{mp} [mA]	167
		V_{mp} [mV]	450
Extracted Parameters	R_s [Ω]	0.22	
	R_{sh} [Ω]	122	
	A	1.72	
	I_{sat} [nA]	238	
	I_{ph} [mA]	188.6	
Analyzed Parameters	PCE [%]	10.5	
	FF [%]	67.8	
	J [mA/cm ²]	23.4	

IV. SC TEMPERATURE ANALYSIS RESULTS IN SC-CPA

The thermal characterization focuses on the energy performance of the SC since for the antenna, as it is passive, there will be no significant change in electromagnetic performance in the observed range [21]. The main component in the analysis is the SC equivalent circuit model, which was simulated on ADS software using the extracted parameters shown in Table II (photogenerated current (I_{ph}), saturation current (I_{sat}), R_s , R_{sh} and the A). The validation of the simulated model is done by comparing the experimental and numerical I-V curves. Fig. 8 shows the power and I-V curves obtained in the laboratory tests and those derived in the ADS software, highlighting the satisfactory agreement between them. Hence, the circuit model is ready to estimate the SC behavior under temperature variable conditions.

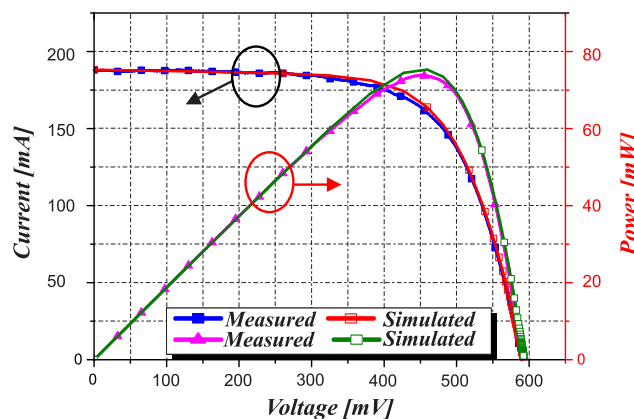


Fig. 8. Simulated and measured I-V and power curves of the SC-CPA for STC.

The dependence between temperature and the current supplied by the SC is given by [22]:

$$I_{pv} = I_{ph} - \underbrace{I_{sat} \left[e^{\frac{V_o + I_{ph} R_s}{AV_t}} - 1 \right]}_{I_d} - \frac{V_o + I_{ph} R_s}{R_{sh}} \quad (4)$$

where V_o is the output voltage, $V_t = KT/q$ is the threshold voltage, being K the constant of Boltzmann, q the electron charge, and I_d the diode current. In the circuit of Fig. 5, I_{ph} is represented as a real current

source, and it has a constant value if the temperature and the irradiance are constant. Nevertheless, its behavior is described by [22]:

$$I_{ph} = \frac{[I_{sc} + k_i(T - T_{ref})] G}{G_{ref}} \quad (5)$$

where k_i is the short-circuit current temperature coefficient, which, for a monocrystalline silicon SC as used in this work, can be considered as 0.035% [22]. T_{ref} and G_{ref} are the reference temperature and irradiance, which are considered to be, respectively, 298 K and 1000 W/m². The expression shown in (5) was used to model the current supplied by the ideal current source that represents I_{ph} in ADS, where it can be seen that, under STC, $I_{ph} = I_{sc}$.

The behavior of the SCA as a function of temperature was analyzed by simulation considering the equivalent circuit model for a constant irradiance of 1000 W/m². The PN junction temperature was changed from 243 to 323 K, and the I_{mp} , V_{mp} , and MPP values were recorded for each temperature. Then, it was possible to calculate the PCE, FF, and J for each condition.

Fig. 9 and Fig. 10 depict, respectively, the I-V and power curves of the SC-CPA for the temperature values T=243, 260, 280, 298, 305, and 323 K. Fig. 9 shows an increase of I_{sc} for higher values of temperature due to the reduction of the bandgap energy (E_g) of the material [1], which is explained by [23]:

$$E_g(T) = E_g(0) - \frac{\alpha T^2}{T + \beta} \quad (6)$$

where $E_g(0) = 1.17\text{eV}$ is the bandgap energy at 0 K, and α and β are constants related to the semiconductor material [23]. On the other hand, it can be seen that V_{oc} decreases significantly as the temperature increases, affecting the overall performance of the SC. A lower $E_g(T)$ rises the intrinsic carrier concentration, increasing I_{sat} , which affects the V_{oc} . The degradation rate is discussed later in this section by analyzing the shift of the FF and the PCE.

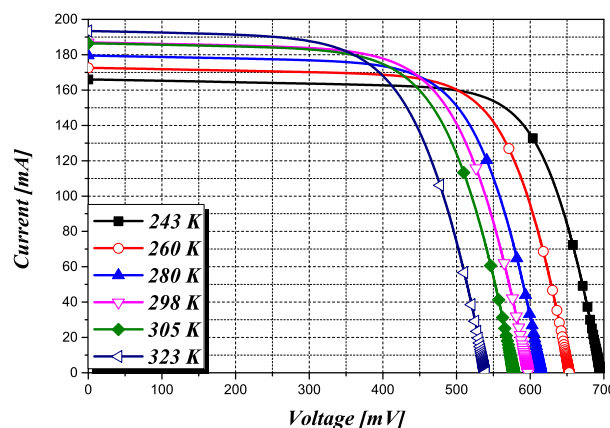


Fig. 9. Temperature influence on the I-V curves of the SC-CPA.

Fig. 10 shows the dependence of the power generated by the SC-CPA as a function of temperature, where it can be seen that the MPP decreases as the temperature increases. The values of V_{mp} , I_{mp} , and MPP for the analyzed range are shown in Fig. 11. The I-V and power curves at 298 K are shown as a reference. The temperature variation in the simulated range shows a shift of approximately 150 mV in

the MPP. Consequently, the power supported at the MPP drops from approximately 83 mW at 243 K to 64 mW at 323 K. Special attention must be given to how the optimal operation point of the SC is changing, even more before reaching cold-start or close to drop under the turn-off voltage thresholds. The calculated temperature variation coefficients for V_{mp} , I_{mp} , and MPP are, respectively, -2.2 mV/K, 0.3 mA/K, and -0.3%/K.

Fig. 12 shows the FF and PCE curves for the analyzed situations. Both parameters have a decreasing temperature coefficient as V_{mp} decreases at a higher rate than I_{mp} increases. Analyzing (1) and (2), it can be noted that PCE and FF are directly proportional to the current and voltage values in the MPP. The calculated temperature variation coefficients for PCE and FF are, respectively, -0.031%/K and -0.12%/K.

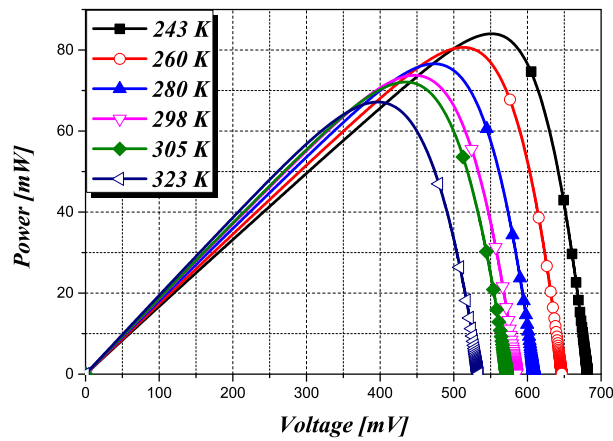


Fig. 10. Influence of the temperature on the power generated by the SC-CPA.

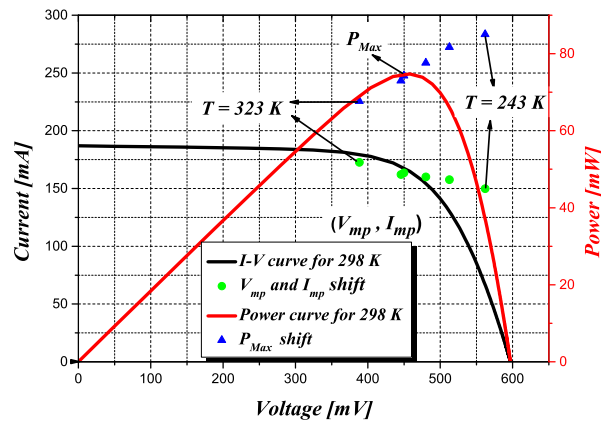


Fig. 11. Variation of V_{mp} , I_{mp} and MPP.

Finally, Table III summarizes the obtained values of the main parameters that characterize the performance of the SC-CPA. It can be seen that J increases proportionally to the number of generated charge carriers. It is also possible to observe that higher temperatures increase the density of carriers in the conduction band following a Fermi-Dirac distribution [24], which produces a larger J when the SC-CPA is polarized.

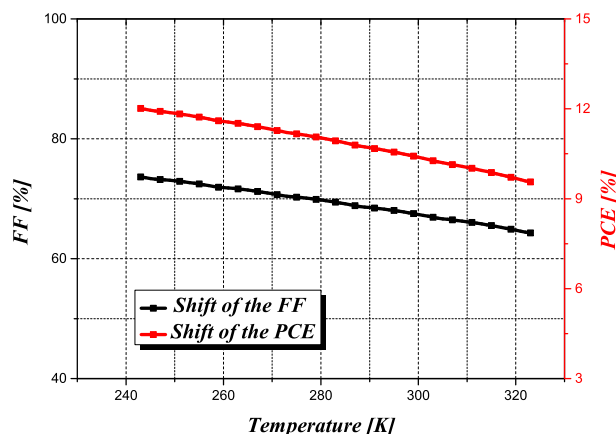


Fig. 12. PCE and FF as a function of temperature.

TABLE III. MAIN SCA PARAMETERS FOR THE SIMULATED CONDITIONS.

Irradiance @ 1000 W/m ²		Temperature [K]						
		243	260	280	298	305	323	
Operation Conditions	I_{sc} [mA]	166	172	179	186	187	193	
	V_{oc} [mV]	693	653	614	592	574	545	
	MPP	I_{mp} [mA]	150	157	159	164	161	172
		V_{mp} [mV]	564	515	475	445	446	386
Analyzed Parameters	PCE [%]	11.9	11.5	11	10.2	10.1	9.4	
	FF [%]	73.6	71.9	69.8	67.4	66.6	64.3	
	J [mA/cm ²]	21.1	22.2	22.5	22.8	23.7	24.3	

V. CONCLUSION

This paper has presented a SCA design, in which the authors proposed and manufactured a patch antenna based on a photoconductive material for IoT and WSN applications. The prototype antenna has provided a 12.7% bandwidth centered at 2.45 GHz and gain of approximately 4.19 dBi at the resonance frequency. The SC-CPA equivalent circuit parameters were used to obtain the I-V and power versus temperature curves and its corresponding MPPs. The shifting rates of the SC-CPA parameters were represented as a function of the corresponding temperature variation coefficients. The authors quantitatively concluded that increasing temperature reduced the PCE and FF despite increasing J . Simulation results showed a 150 mV shift of the SC MPP for the observed temperature range, representing a decrease of approximately 20 mW from the lower temperature (243 K) to the maximum (323 K). The higher the temperature, the lower is the voltage and power supported. The results obtained highlight that temperature variations in a low-power SC can significantly influence its performance. Special attention must be given to the MPP, even more, if this value is under cold-start or close to the turn-off voltage threshold. On the other hand, a satisfactory PCE of 10.2 % of the SC can supply 445 mV and 164 mA (≈ 73.1 mW) at 298 K. Finally, the proposed structure has proved to be a potential solution for sensor networks as a hybrid structure, including an energy source and antenna for communications.

ACKNOWLEDGMENTS

This research was partially supported by INERGE, CNPq (309848/2018-0), FAPESP (2019/25866-7), and CAPES (Finance Code 001). The authors would like to thank Prof. A. S. Polo of UFABC for

supporting the SC measurement setup.

REFERENCES

- [1] S. Ponce-Alcantara, J. P. Connolly, G. Sanchez, J. M. Maguez, V. Hoffmann, and R. Ordas, "A statistical analysis of the temperature coefficients of industrial silicon solar cells," *Energy Procedia*, vol. 55, pp. 578 – 588, 2014, Proceedings of the 4th International Conference on Crystalline Silicon Photovoltaics (SiliconPV 2014).
- [2] Y. Chen, N. Chiotellis, L. Chuo, C. Pfeiffer, Y. Shi, R. G. Dreslinski, A. Grbic, T. Mudge, D. D. Wentzloff, D. Blaauw, and H. S. Kim, "Energy-autonomous wireless communication for millimeter-scale internet-of-things sensor nodes," *IEEE Journal on Selected Areas in Communications*, vol. 34, no. 12, pp. 3962–3977, Dec 2016.
- [3] A. Narbudowicz, O. O'Conchubhair, M. J. Ammann, and D. Heberling, "Integration of antennas with sun-tracking solar panels," *Electronics Letters*, vol. 52, no. 15, pp. 1325–1327, 2016.
- [4] O. O'Conchubhair, A. Narbudowicz, P. McEvoy, and M. J. Ammann, "Circularly polarised solar antenna for airborne communication nodes," *Electronics Letters*, vol. 51, no. 9, pp. 667–669, 2015.
- [5] N. Ullah and A. Tekin, "Omni-directional wideband antenna array with solar cells," *Journal of Microwaves, Optoelectronics and Electromagnetic Applications*, vol. 20, no. 1, pp. 60 – 75, 2021.
- [6] E. V. V. Cambero, H. P. d. Paz, V. S. d. Silva, H. X. d. Araújo, I. R. S. Casella, and C. E. Capovilla, "2.4 GHz Coplanar Patch Antenna with Solar Cell as Radiator for Communication and Energy Harvesting," in *2019 SBMO/IEEE MTT-S International Microwave and Optoelectronics Conference (IMOC)*, pp. 1–3, 2019.
- [7] E. V. V. Cambero, H. P. da Paz, V. S. da Silva, H. X. de Araujo, I. R. S. Casella, and C. E. Capovilla, "A 2.4 GHz rectenna based on a solar cell antenna array," *IEEE Antennas and Wireless Propagation Letters*, vol. 18, no. 12, pp. 2716–2720, Dec 2019.
- [8] O. O'Conchubhair, K. Yang, P. McEvoy, and M. J. Ammann, "Amorphous silicon solar vivaldi antenna," *IEEE Antennas and Wireless Propagation Letters*, vol. 15, pp. 893–896, 2016.
- [9] E. V. V. Cambero, H. P. da Paz, V. S. da Silva, H. X. de Araujo, I. R. S. Casella, and C. E. Capovilla, "On the influence of area variations of the photovoltaic surface in solar cell antennas," in *15th Brazilian Power Electronics Conference and 5th IEEE Southern Power Electronics Conference*, pp. 450–455, 2019.
- [10] Y. Tawk, J. Costantine, F. Ayoub, and C. G. Christodoulou, "A communicating antenna array with a dual-energy harvesting functionality [wireless corner]," *IEEE Antennas and Propagation Magazine*, vol. 60, no. 2, pp. 132–144, April 2018.
- [11] O. Yurduseven and D. Smith, "Solar cell stacked dual-polarised patch antenna for 5.8 GHz band WiMAX network," *Electronics Letters*, vol. 49, no. 24, pp. 1514–1515, 2013.
- [12] O. Yurduseven, D. Smith, and M. Elsdon, "UWB meshed solar monopole antenna," *Electronics Letters*, vol. 49, no. 9, pp. 582 –584, 2013.
- [13] T. Yekan and R. Baktur, "Conformal integrated solar panel antennas: Two effective integration methods of antennas with solar cells," *IEEE Antennas and Propagation Magazine*, vol. 59, no. 2, pp. 69–78, Apr 2017.
- [14] ENF-Solar, "NS6QL Black 21 Datasheet," <https://www.enfsolar.com/pv/cell-datasheet/2039>, n.d., last Check February 11rd 2021.
- [15] K. Et-torabi, I. Nassar-eddine, A. Obbadi, Y. Errami, R. Rmaily, S. Sahnoun, A. E. fajri, and M. Agunaou, "Parameters estimation of the single and double diode photovoltaic models using a Gauss-Seidel algorithm and analytical method: A comparative study," *Energy Conversion and Management*, vol. 148, pp. 1041 – 1054, 2017.
- [16] C. A. Balanis, *Antenna theory: analysis and design*. Wiley-Interscience, 2005.
- [17] P. F. Fonseca, Daniel and Vitor, "Study of patch antennas with koch curve form slots," *Journal of Microwaves, Optoelectronics and Electromagnetic Applications*, vol. 18, no. 3, pp. 399 – 407, 2019.
- [18] H. Nishimoto, Y. Kawahara, and T. Asami, "Prototype implementation of ambient rf energy harvesting wireless sensor networks," in *Sensors, 2010 IEEE*, pp. 1282–1287, 2010.
- [19] A. K. Singh, S. R. Kasjoo, and A. Song, "Coplanar waveguide fed coplanar patch antenna for nanorectifiers at 2.45GHz," *Progress in Electromagnetics Research Symposium*, pp. 2386 – 2389, 2015.
- [20] K. Mehrotra, C. Mohan, and S. Ranka, *Elements of Artificial Neural Networks*. The MIT Press, 10 1996. [Online]. Available: <https://doi.org/10.7551/mitpress/2687.001.0001>
- [21] A. Collado and A. Georgiadis, "Conformal hybrid solar and electromagnetic (em) energy harvesting rectenna," *IEEE Transactions on Circuits and Systems I: Regular Papers*, vol. 60, no. 8, pp. 2225–2234, Aug 2013.
- [22] A. Gontean, S. Lica, S. Bularka, R. Szabo, and D. Lascu, "A novel high accuracy PV cell model including self heating and parameter variation," *Energies*, vol. 11, no. 1, 2018.

- [23] H. Zhang, X. Qiao, Y. Shen, and M. Wang, "Effect of temperature on the efficiency of organometallic perovskite solar cells," *Journal of Energy Chemistry*, vol. 24, no. 6, pp. 729 – 735, 2015.
- [24] S. Chander, A. Purohit, A. Sharma, Arvind, S. Nehra, and M. Dhaka, "A study on photovoltaic parameters of monocrystalline silicon solar cell with cell temperature," *Energy Reports*, vol. 1, pp. 104 – 109, 2015.

ERRATA

On page 194, the paper title in the original version was incorrectly given:

Simulation of Temperature Effects in a 2.4 GHz Coplanar Solar Cell Patch Antenna Prototype

The correct title is:

A 2.4 GHz Coplanar Solar Cell Patch Antenna with a Semi-Analytical Evaluation of Temperature Effects